applied sciences

MDPI

Article

Mechanical Properties and Failure Mechanism of Granite with Maximum Free Water Absorption under Triaxial Compression

Yaoyao Zhang [1,2], Yangbing Cao [1,2,*], Zhijun Li [3], Yangtao Chen [1] and Zhenping Huang [1]

[1] Zijin School of Geology and Mining, Fuzhou University, Fuzhou 350108, China; zyy76700922@163.com (Y.Z.); cyt19940123@163.com (Y.C.); zhphuang@126.com (Z.H.)
[2] Key Laboratory of Geohazard Prevention of Hilly Mountains, Ministry of Natural Resources (Fujian Key Laboratory of Geohazard Prevention), Fuzhou 350003, China
[3] Beijing New Oriental Star Engineering Investigation Design Co., Ltd., Beijing 100070, China; lizhijun_bnec@163.com
* Correspondence: ybcao@fzu.edu.cn

Abstract: Granite in underground water-sealed storage caverns has usually been immersed for a long time. The immersion affects the mechanical properties and failure mechanism of granite with maximum free water absorption; therefore, it is crucial to study the behavior of granite under different confining pressures for engineering construction. A triaxial compression test with maximum free water absorption was conducted on granite and its mechanical properties were analyzed. A fracture scanning electron microscope test was carried out to analyze the microstructural characteristics and reveal the failure mechanism. The test results showed that the differential stress-axial strain curve can be divided into the initial compaction stage, the elastic deformation stage, the plastic deformation stage, and the post-peak strain-softening stage. With an increase in confining pressure, the duration of the initial compaction stage decreased, while the plastic deformation stage and the peak strength and peak strain stages increased. For the confining pressure range of 0–20 MPa, the peak stress difference of granite with maximum free water absorption was between 146.0 and 307.6 MPa. The elastic modulus was between 31.36 and 44.18 GPa. The cohesion (c) of the rock sample studied was 26.84 MPa and the internal friction angle (φ) was 51°. The failure mechanism of granite is tensile–shear composite failure, predominantly with tensile failure under low confining pressure regimes, and the inclined fracture surface is mainly due to shear failure under high confining pressure conditions. These research results provide updated reference data for rock engineering involving granitic mechanical properties and failure mechanisms in submerged caverns.

Keywords: granite; confining pressure; water absorption; mechanical properties; failure mechanism

Citation: Zhang, Y.; Cao, Y.; Li, Z.; Chen, Y.; Huang, Z. Mechanical Properties and Failure Mechanism of Granite with Maximum Free Water Absorption under Triaxial Compression. *Appl. Sci.* **2022**, *12*, 3930. https://doi.org/10.3390/app12083930

Academic Editors: Xiaoping Zhou, Hao Cheng, Yundong Shou and Junwei Chen

Received: 8 March 2022
Accepted: 11 April 2022
Published: 13 April 2022

1. Introduction

Underground water-sealed storage cavern projects are mostly built in granite host rock and have high exacting requirements for the mechanical properties of the surrounding rock. The granite in such underground water-sealed storage caverns has been immersed in water for a long time, allowing pervasive water absorption. When granite absorbs the maximum free water content, the stability of the engineering rock mass is negatively affected. At the same time, different burial depths of the caverns result in different confining pressures of the rock mass. Therefore, it is of great significance to study the mechanical properties and failure mechanisms of granite with maximum free water absorption under different confining pressures for this type of engineering construction.

At present, research on the triaxial compression of granite block mainly focuses on the basic mechanical properties and failure characteristics. Yang et al. [1] summarized the stress-strain relationship of rock under the conditions of the conventional triaxial compression test, improved the classical plastic statistical damage model, and preliminarily verified the constitutive relationship expression by using the results of the conventional triaxial

compression test. Xie et al. [2] proposed a nonlinear empirical strength criterion based on Mohr–Coulomb criterion, which provides a new reference and method for determination of the triaxial compressive strength of rock materials. Zhou et al. [3] conducted triaxial compression tests under different confining pressures to study the deformation and failure characteristics and mechanisms of granite. Lajtai [4] believed that the deformation mechanism of granite includes elastic deformation, brittle deformation, and compaction deformation. The latter two deformations are related to micro-fractures. Chen et al. [5] used acoustic emission technology to carry out conventional triaxial compression tests on granite under different temperatures and confining pressures, and carried out damage analysis and characteristic stress value analysis. Zhu et al. [6] studied the mechanical properties of Dagangshan granite using static triaxial tests and dynamic triaxial tests, indicating that the compressive strength, Poisson's ratio, and elastic modulus of granite are related to the strain rate. Du et al. [7–9] studied the mechanical properties of granite after high temperature exposure and found that the peak strength and elastic modulus of granite after high temperature exposure decreased sharply. The P-wave velocity also decreased to varying degrees. Yao et al. [10–12] conducted uniaxial and triaxial compression tests on intact granite as well as single-and double-defect granite specimens, and further studied the influence of confining pressure and fracture on rock strength and failure mode. Zhao et al. [13–16] studied the failure process, strength characteristics, and damage evolution mechanism of Beishan granite under different confining pressures. Dai et al. [17] studied the damage evolution characteristics of granite during loading and unloading through a series of triaxial tests under different confining pressures. Ji et al. [18–21] studied the deformation and acoustic emission characteristics of granite under different confining pressures using triaxial compression tests. Wang et al. [22] studied the triaxial compression mechanical properties of granite under chemical corrosion. Sun et al. [23] studied the mechanical properties of granite after the peak stage and found that after the peak, the rock exhibited plastic failure characteristics under confining pressure. Li et al. [24] studied the microscopic process of the progressive failure of granite plates and found that the occurrence and development of axial cracks eventually led to the splitting failure of the samples. Zhang et al. [25] conducted triaxial compression tests of marble and granite under different confining pressures, proposed a damage index (DI) to describe the degree of damage to marble in the post-peak stage, and established a quantitative relationship between the rock fracture angle and confining pressure. In addition, Cheng et al. [26–28] studies show that crack openings significantly affect the crack initiation stresses and crack initiation modes, and propose a new method for the simulation of frictional contact on crack slips in the framework of the XFEM. In addition, nuclear magnetic resonance (NMR) measurements are carried out to evaluate the micro-cracking characteristics of sandstones during the creep stage under the different levels of creep stresses.

For related research on granite under different water-bearing states, Koji Masuda [29] studied the dry and wet failure strengths of granite and andesite under different strain rates and confining pressure conditions. Li et al. [30] carried out a study on the rheological properties of water-saturated granite under uniaxial compression. The study showed that the long-term strength of water-saturated granite was significantly reduced and the rheological rate and degree of deformation were significantly increased. Deng et al. [31] carried out three-point bending tests on two types of deep granite with different water contents. The results show that the fracture mechanics and acoustic emission characteristics of granites undergo significant changes under the influence of water. Cao et al. [32,33] studied the brittleness characteristics of granite with different degrees of water saturation using new evaluation indices combined with uniaxial compression tests. They also carried out fracture scanning electron microscopy (SEM) and analyzed the microscopic granular morphology to reveal the failure mechanism.

At present, there are few studies on the mechanical properties and failure mechanism of granite under the background of water-sealed storage cavern engineering. There are few studies on the maximum free water absorption characteristics of granite, its triaxial

compression failure mechanism, and the differences in the stress conditions under different engineering environments. In this study, a laboratory triaxial compression test of granite with maximum free water absorption under different confining pressures was carried out, and the failure mechanism of the rock mass was obtained from the microscopic topography through SEM. The data collected in this study can provide reference data for related rock mass engineering and research.

2. Experimental Scheme

2.1. Sample Preparation

A complete crack-free granite block was extracted from an underground water-sealed storage cavern in Shandong province, China, and cylindrical rock samples with a diameter of 50 mm and an aspect ratio of 2 were obtained from this material. Some of the samples are shown in Figure 1. The stipulations of the *Standards for Engineering Rock Mass Test Methods* [34] were followed to ensure the representativeness and accuracy of each sample after processing.

Figure 1. Demonstration photographs of some samples.

In the water absorption test, the sample mass and P-wave velocity did not change when the maximum free water absorption was reached. To avoid affecting the characteristics of the sample, a water absorption test was carried out without drying. The test results are shown in Figure 2. The trend of the water absorption curve of each sample was similar. Within 42 h, the free water absorption of the granite changed significantly, and the free water absorption, W_a, increased from 0% to 0.150%. Owing to the density of the granite, low porosity, and slow water absorption, the initial water absorption of the rock sample increased rapidly. With the increase in water content in the pores, the water absorption growth rate gradually slowed down. From 306 h to 546 h, the free water absorption of the rock samples was essentially unchanged. Therefore, the water absorption test was stopped after 546 h, when the granite samples had reached the maximum free water absorption.

The test results of P-wave velocity are shown in Figure 3 and were between 3350 and 4850 m/s. In the initial 6 h, the P-wave velocity increased rapidly. It can be seen from the water absorption test that the water absorption rate also increased rapidly during this period. When the water content in the pores increased to a certain value, the water absorption capacity of the rock sample decreased but continued to increase slowly, along with a slow increase in P-wave velocity. After 210 h, the P-wave velocity gradually tended to stabilize; however, because the water absorption still had some fluctuation, the sample reached maximum free water absorption after 546 h.

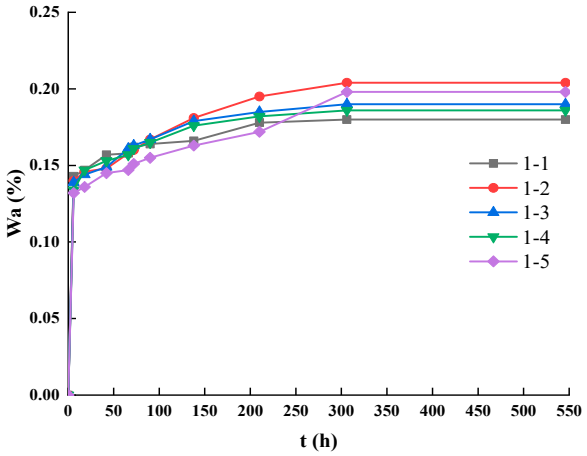

Figure 2. Diagram of sample water absorption changing with immersion time.

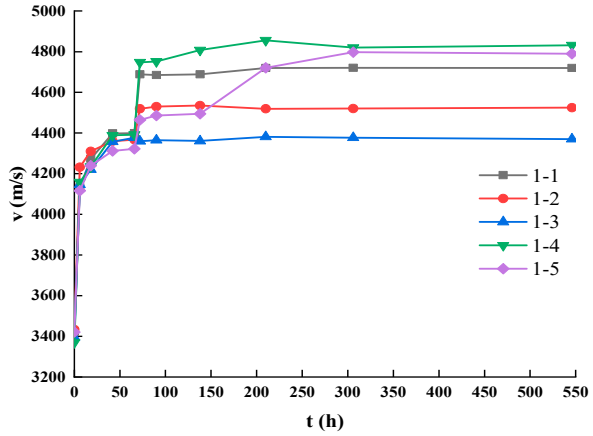

Figure 3. Curve diagram of P-wave velocity of sample changing with water immersion time.

2.2. Testing the Confining Pressure and Parameter Setting

The confining pressure during the triaxial compression test of the sample was determined according to the burial depth conditions of the storage cavern site. Groundwater-sealed storage cavern reservoirs were selected in coastal granite areas with stable groundwater levels where the surrounding rock integrity was relatively good and the surrounding rock quality grade was generally high. According to the in-situ stress measurement results of the water pressure fracturing method in a typical water-sealed storage cavern site built in China and through the tensor analysis and linear regression analysis, the fitted formulas of principal stress and elevation are as follows (the compressive stress is negative; σ_H is the maximum principal stress and the unit is MPa; σ_h is the intermediate principal stress and the unit is MPa; σ_v is the minimum principal stress and the unit is MPa; h is the elevation and the unit is m):

$$\begin{cases} \sigma_H = 0.0347h - 7.2014 \\ \sigma_h = 0.0192h - 4.9748 \\ \sigma_v = 0.026h - 1.82 \end{cases} \quad (1)$$

Confining pressure is set by the burial depth of the storage cavern. The maximum burial elevation of the typical water-sealed storage cavern built in China is −146 m, so h is equal to −146 m. According to the above fitting formula, σ_H is equal to −12.3 MPa, σ_h is equal to −7.8 MPa, and σ_v is equal to −5.6 MPa. Considering the access tunnel with a shallower burial depth and the shaft with a deeper burial depth, the confining pressure range is appropriately expanded. The final confining pressures are 0 MPa, 5 MPa, 10 MPa, 15 MPa, and 20 MPa.

A total of 15 samples were selected for triaxial compression test research and divided into five groups according to different confining pressures, with three samples in each group. The instrument used in the triaxial compression test was a TAJW–2000 rock mass multi-field coupling triaxial test system (Figure 4). The stress control method was used to increase the confining pressure at a rate of 0.05 MPa/s until the specified confining pressure [34]. After the confining pressure was stabilized, the specimen was loaded to failure at a displacement rate of 0.003 mm/s.

Figure 4. TAJW–2000 rock mass multi-field coupling triaxial test system.

3. Mechanical Properties Analysis

3.1. Stress-Strain Curve Features

The overall results of the laboratory tests are shown in Table 1. Due to small data deviations, the subsequent analysis was carried out by taking the average value or eliminating the abnormal value.

Table 1. The test results of granite with different confining pressures and water contents.

No.	Confining Pressure (MPa)	Water Content (%)	Peak Differential Stress (MPa)	Average Peak Differential Stress (MPa)	Elastic Modulus (GPa)	Average Elastic Modulus (GPa)
1-1	0	0.180	147.0	146.0	31.84	31.36
1-2		0.204	141.0		31.09	
1-3		0.184	149.0		31.14	
2-1	5	0.190	191.4	190.8	39.85	38.84
2-2		0.186	190.1		37.82	
2-3		0.198	238.6		47.45	
3-1	10	0.233	224.6	226.0	37.95	39.18
3-2		0.176	226.8		42.61	
3-3		0.191	226.5		36.99	
4-1	15	0.213	265.1	262.6	41.75	40.20
4-2		0.200	261.0		39.41	
4-3		0.187	261.6		39.45	
5-1	20	0.160	291.3	287.6	45.33	44.18
5-2		0.161	291.0		44.26	
5-3		0.155	280.4		42.96	

The typical differential stress-axial strain curves under different confining pressures are shown in Figure 5, where σ_1 is axial stress, σ_3 is confining pressure, (σ_1–σ_3) is differential stress, and ε_1 is axial strain. The curves can be divided into the initial compaction stage (upper concave section), elastic deformation stage (straight line section), plastic deformation stage (non–linear section before peak value), and post-peak strain-softening stage. As the

confining pressure increases, the initial compaction stage becomes smaller and smaller, indicating that the sample becomes denser under the action of confining pressure. With the increase in confining pressure, the plastic deformation stage before the peak becomes longer, indicating that the plastic properties of the sample are obvious with an increase in the confining pressure. The peak differential stress increases and the peak axial strain slightly increases with an increase in the confining pressure, indicating that an increase in the confining pressure makes the strength of the rock gradually increase.

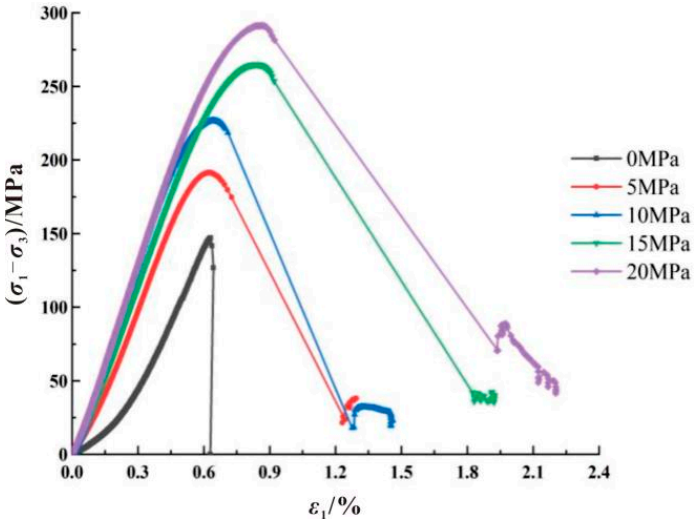

Figure 5. Typical granite differential stress-axial strain curves under different confining pressures.

The granite samples showed obvious brittle failure under low confining pressure. When the confining pressure was 0 MPa, the peak strain of the sample was 0.60–0.65% and the peak axial stress was between 141–149 MPa. When the confining pressure was 5 MPa, the peak axial strain of the sample was 0.63–0.72% and the peak differential stress was between 190–192 MPa. As shown in Figure 5, under the condition of low confining pressure, as the confining pressure increased, the initial compaction stage became significantly smaller. That is, the initial concave part of the curve became significantly smaller.

The granite exhibits characteristics of plastic failure under medium and high confining pressures. When the confining pressure was 10 MPa, the peak axial strain of the sample was 0.70–0.90% and the peak differential stress was 224–226 MPa. When the confining pressure was 15 MPa, the peak axial strain of the sample was 0.91–1.00% and the peak differential stress was 261–265 MPa. When the confining pressure was 20 MPa, the peak axial strain of the sample was 0.92–1.03% and the peak differential stress was 280–292 MPa. As shown in Figure 5, as the confining pressure increased, the initial compaction stage gradually decreased; that is, the initial upward concave part of the curve in Figure 5 gradually decreased; as the confining pressure increased, the peak axial strain of the sample gradually increased and the peak differential stress increased significantly. The microcracks in the sample were compressed gradually and closed, resulting in nonlinear deformation. As shown in Figure 5, the sample did not reach peak strength. It will be destroyed immediately but lost its bearing capacity once the strength decreased slightly. The brittleness of the granite gradually decreased, showing obvious plastic failure characteristics. The higher the confining pressure, the more obvious the plastic failure characteristics were.

3.2. Deformation and Strength Properties

According to the results of the triaxial compression test, the elastic modulus and peak differential stress of granite under different confining pressures are shown in Figures 6 and 7. The elastic modulus of granite under the maximum free water absorption rate when the confining pressure is in the range of 0–20 MPa is between 31.36 and 44.18 GPa and the axial stress is between 146.0 and 307.6 MPa.

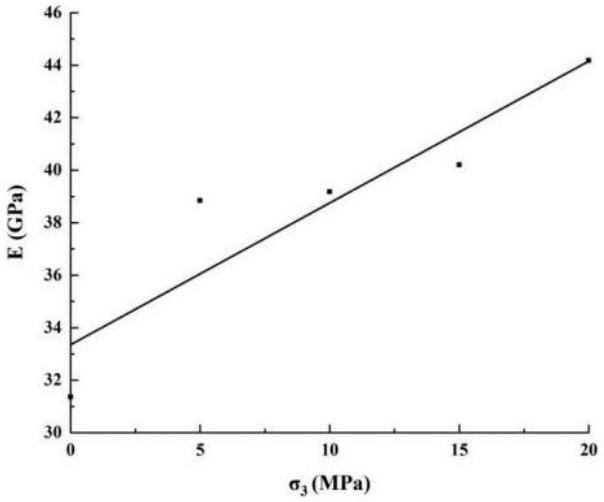

Figure 6. The curve of elastic modulus E changes with confining pressure.

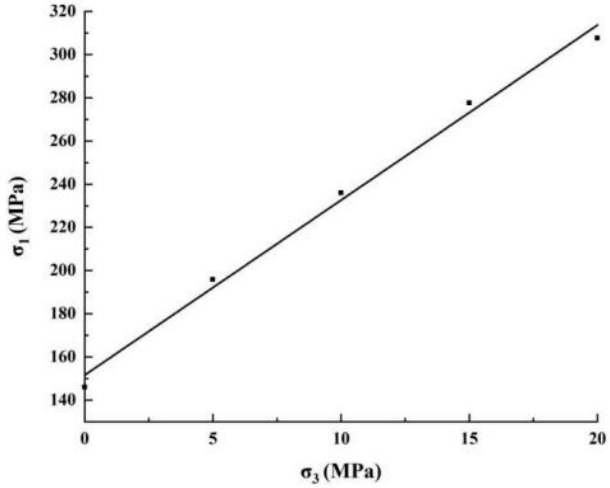

Figure 7. The curve of axial stress changes with confining pressure.

The elastic modulus E and confining pressure σ_3 are approximately linearly correlated as shown in Figure 6, which can be expressed by the fitting function (Equation (2)), using a correlation factor of 0.844.

$$E = 33.352 + 0.54\sigma_3 \quad \left(R^2 = 0.844\right) \tag{2}$$

The axial stress and confining pressure also increase approximately linearly (Figure 7), as shown in the fitting function (Equation (3)), using a correlation factor of 0.993.

$$\sigma_1 = 151.6 + 8.1\sigma_3 \quad \left(R^2 = 0.993\right) \tag{3}$$

According to the Mohr–Coulomb strength criterion and the fitting of Equation (3) (m = 8.1, b = 151.6), the internal friction angle (φ = 51°) and cohesion (c = 26.84 MPa) were calculated.

Using the Hoek–Brown strength criterion, it was found that the rock sample used in this test was a complete rock block; therefore, s = 1 was assigned. According to the uniaxial compression test, σ_c = 146 MPa, and by fitting the triaxial compression test data, m = 21.42, α = 0.499, the fitting formula is shown in Equation (4) and the fitting curve is shown in Figure 8. From the above analysis, the fitting effect of the Hoek–Brown criterion

was demonstrated to be superior to that of the Mohr–Coulomb criterion, indicating that the rock sample had slight nonlinear characteristics.

$$\sigma_1 - \sigma_3 = (3127.32\sigma_3 + 21,316)^{0.499} \quad \left(R^2 = 0.999\right) \tag{4}$$

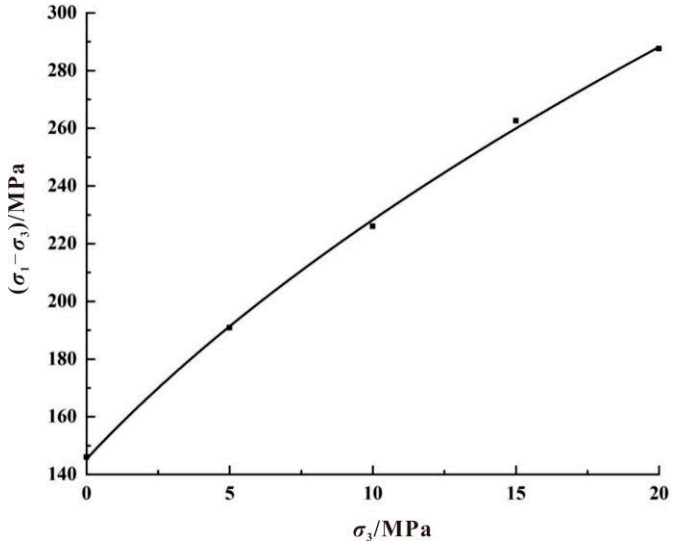

Figure 8. The fitting curve using Hoek–Brown strength criterion.

3.3. Macroscopic Failure Characteristics and Fracture Surface Morphology

3.3.1. Low Confining Pressure Conditions (0 and 5 MPa)

The failure diagram with confining pressure at 0 MPa, is shown in Figure 9. There was no phenomenon in the sample for a long time. With continuous application of the load, microcracks were gradually generated and then the clear and brittle sound of the rock sample cracking could be heard; however, the surface of the rock sample was not destroyed, but particle ejection occurred at the corner of the rock sample, producing flake spalling debris. With continuous loading, the microcracks continued to extend from both ends to the middle. Finally, the microcracks became interconnected; the rock sample lost its bearing capacity instantly and collapsed loudly.

The relevant failure diagrams for confining pressure at 5 MPa are shown in Figure 10. Owing to the confining pressure, the original fractures compacted and the mechanical properties of the rock samples improved. It can be observed from the fracture surface that the integrity of the sample was good after failure and the sample damage was localized along a fracture surface inclined at an angle between 69° and 74°. There is also a fracture surface of approximately 90°, resulting in vertical fracture fragments.

Figure 9. *Cont.*

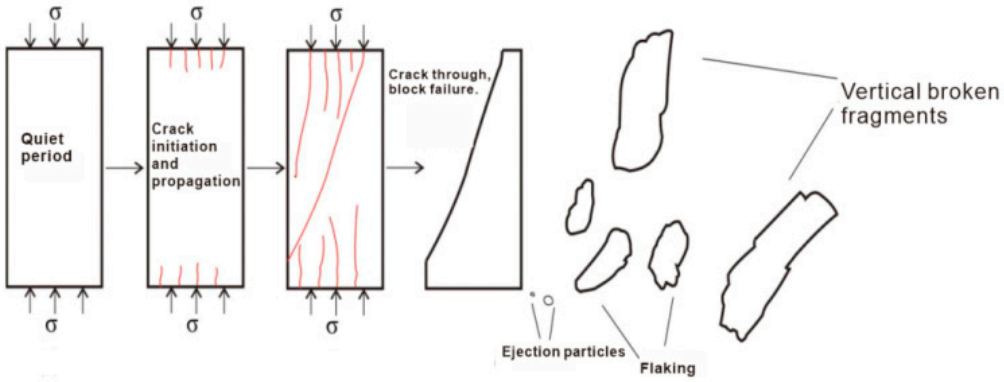

Figure 9. Test results and failure modes of granite with confining pressure at 0 MPa.

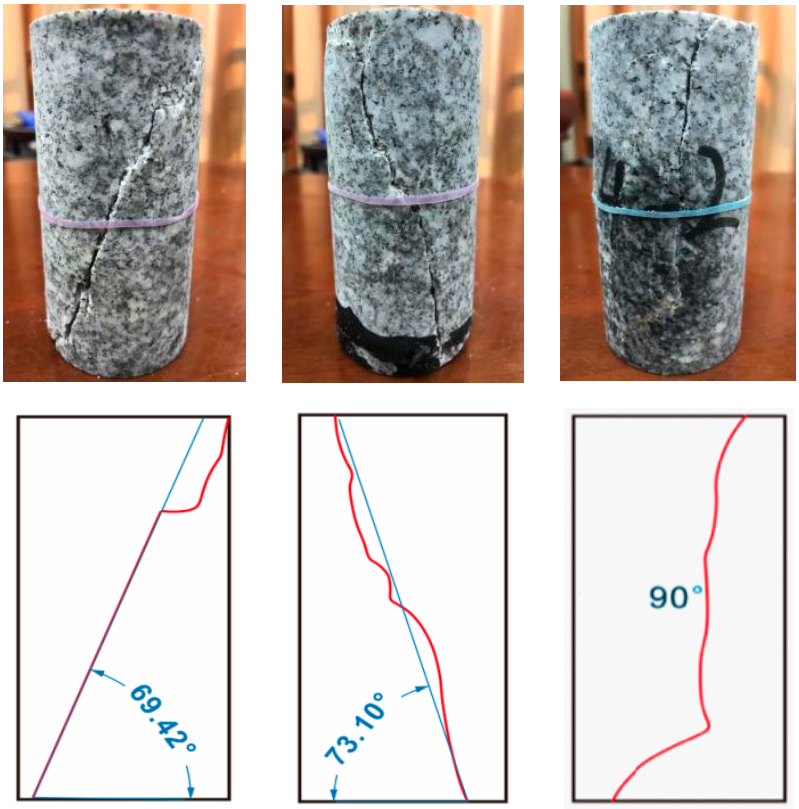

Figure 10. Test results and failure modes of granite with confining pressure at 5 MPa.

3.3.2. Medium and High Confining Pressure Conditions (10, 15, and 20 MPa)

The failure diagrams for scenarios where the confining pressure was 10 MPa is shown in Figure 11. A further increase in the confining pressure made the rock sample denser, and the sample remained complete after failure. The inclined fracture surface was generated along the inclined plane at a certain angle, and the inclination angle of the fracture surface was mostly within the range of 61–71°.

Figure 12 shows the failure diagrams when the confining pressure was 15 MPa. A further increase in the confining pressure further limited the lateral deformation of the specimen, and the specimen after failure remained complete. The fracture surface of the specimen was inclined, and the inclination angle of the fracture surface was 56–68°. It was found that conjugate inclined fracture surfaces formed in some samples with the inclination angles of the two fracture surfaces being approximately the same.

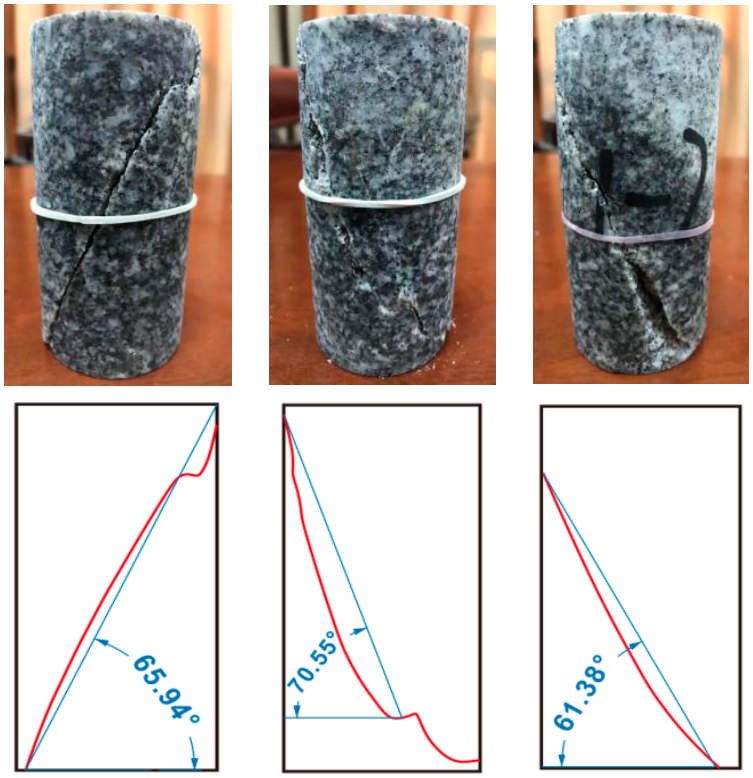

Figure 11. Test results and failure modes of granite with confining pressure at 10 MPa.

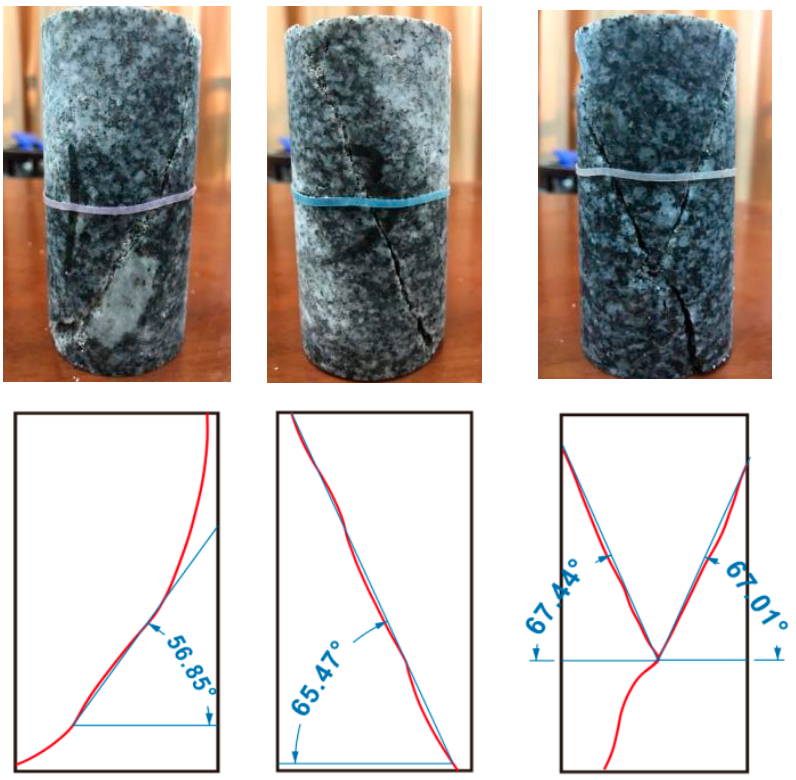

Figure 12. Test results and failure modes of granite with confining pressure at 15 MPa.

Figure 13 shows the failure diagrams for confining pressures at 20 MPa. The specimen was initially in a quiet period for longer than the other cases. The specimen remained

intact after failure and the dip angle of the fracture surface was mostly 61–65°. Some rock samples also produced a conjugate inclined fracture surface.

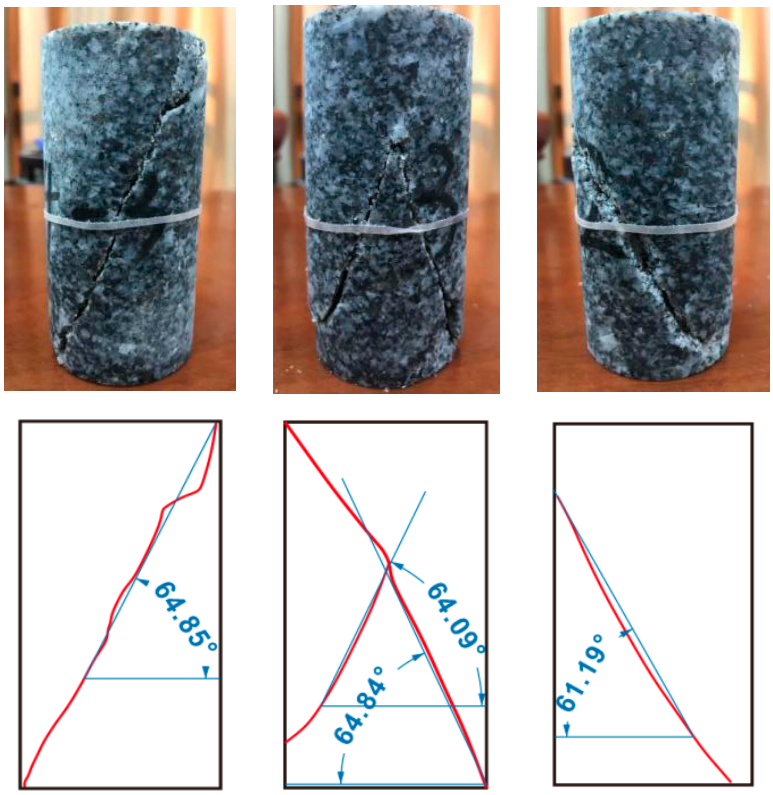

Figure 13. Test results and failure modes of granite with confining pressure at 20 MPa.

Through a study on the failure characteristics and fracture surface morphology of granite under triaxial compression with different confining pressures, it was found that the vertical fracture surface was dominant under low confining pressures, the inclined fracture surface was dominant under medium and high confining pressures, and the dip angle of the fracture surface decreased with the increase in confining pressure. The average angle of the fracture surface decreased from 66° (10 MPa) to 65° (15 MPa) to 63° (20 MPa).

4. Failure Mechanism of Granite under Triaxial Compression

4.1. Microscopic Failure Mechanism of Typical Fracture Surface

To reveal the failure mechanism of granite with maximum free water absorption, combined with the macro failure process and characteristics, typical fracture fragments were selected for SEM to analyze its micro failure mechanism. According to the existing research results [35–40], the typical micromorphology of tensile failure includes intergranular–transgranular fractures (two basic failure patterns), as well as river, root, tongue, and a step pattern without powder. The typical micromorphologies indicating shear failure include intergranular cut crystal rubbing (basic failure pattern), a step pattern containing powder, a parallel slip line pattern, and a parallel stripe pattern, etc.

In this study, flake spalling fragments and vertical fracture fragments produced under low confining pressures and inclined fracture fragments produced under medium and high confining pressures were selected as typical fragments. The fracture micromorphology was tested and analyzed based on SEM data.

4.1.1. Flake Spalling Debris

As shown in Figure 14, Figure 14a shows transgranular pull-out, mineral crystals are broken, and step-like patterns can be seen. Figure 14b,c shows step-like broaching and no

powder accumulation on the steps, and the fracture surfaces are uneven. Sometimes, it can be seen that the broken mineral crystals are scattered on the steps and the above are the typical morphology of tensile failure. In addition, shear failure characteristics were observed on the fracture surfaces of flake spalling fragments. In Figure 14d, the stepped scratches were visible and the powder fragments were stacked on the steps. This indicates that the flake spalling debris is a tensile–shear comprehensive failure mechanism in which there is one main tensile failure and local existence of shear failure.

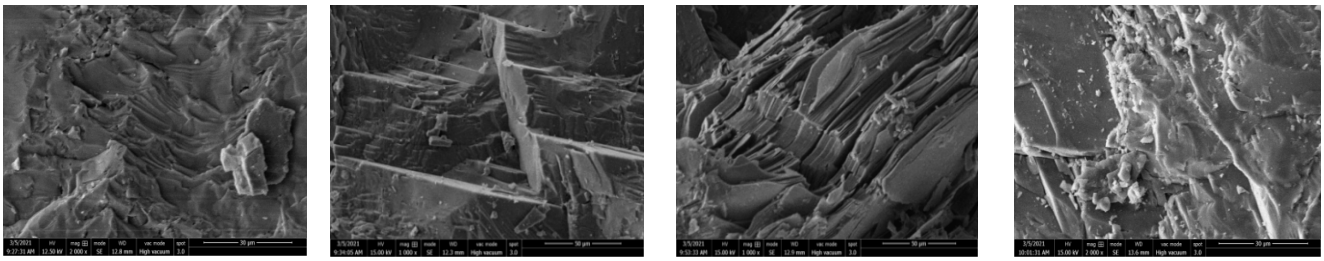

(**a**) (**b**) (**c**) (**d**)

Figure 14. Typical microscopic morphology of flaky exfoliated fragments. (**a**) Broach-step pattern; (**b**) Step pattern; (**c**) Step pattern; (**d**) Stepped flowers.

4.1.2. Vertical Rupture Fragments

The following conclusions can be obtained from Figure 15: Figure 15a shows that the mineral crystal is broken, which is a typical transgranular pull flower. Figure 15b shows that the mineral crystal is not broken, except along the cement around the grain. In Figure 15c, a step-like drawing can be seen. There is no powder accumulation on the step, mineral crystals are broken, and the fracture is uneven. The morphology observed above is typical tensile failure morphology. In addition, shear failure characteristics were observed on the fracture surface of flake spalling debris. In Figure 15d, a large number of rock fragments and powders are visible. Overall, most of the above morphology is typical tensile failure morphology and typical local shear failure morphology, indicating that the vertical fracture debris is a tensile–shear comprehensive failure mechanism, mainly tensile failure and local shear failure.

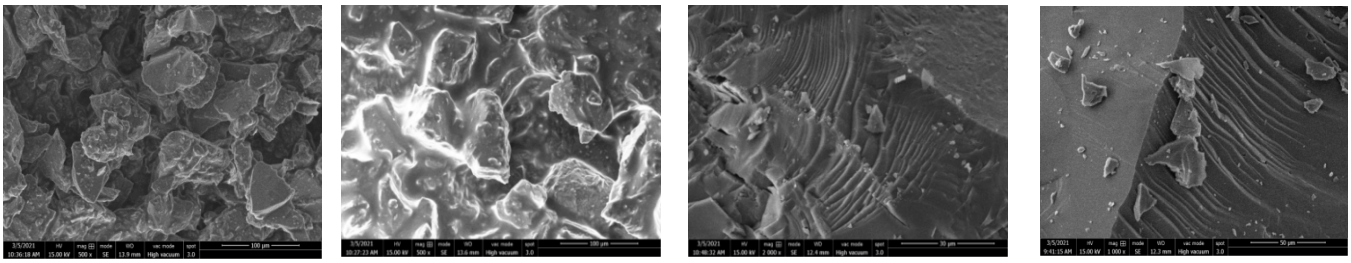

(**a**) (**b**) (**c**) (**d**)

Figure 15. Typical microscopic morphology of vertical fracture fragments. (**a**) Transgranular pull flowers; (**b**) Flowering along crystal; (**c**) Step pattern; (**d**) Stepped flowers.

4.1.3. Inclined Rupture Fragments

The following results can be obtained by observing Figure 16: Figure 16a,b show the grazed pattern. Figure 16c is a parallel stripe pattern, which is formed by friction on the broken surface. The above observed morphologies are typical shear failure morphologies. In addition, tensile failure characteristics were observed on the fracture surface of the inclined fracture fragments, such as the transgranular broaching in Figure 16d. In summary, most of the morphology is typical of shear failure and the local tensile failure is typical. It

shows that the inclined fracture debris is a comprehensive tensile–shear failure mechanism and the shear failure is the main failure mode.

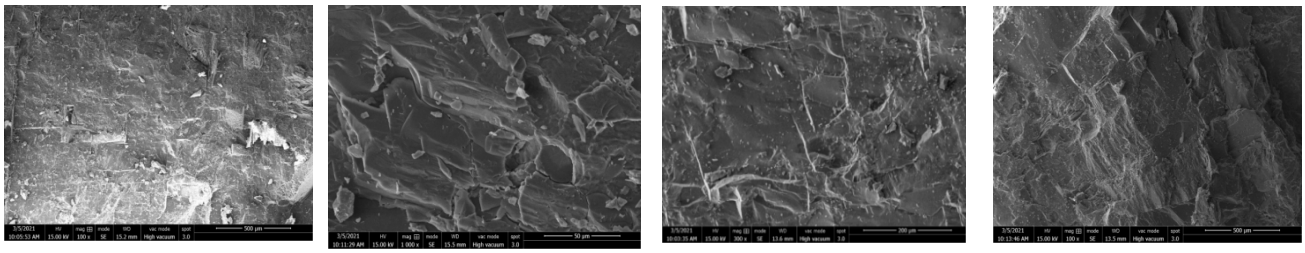

(**a**) (**b**) (**c**) (**d**)

Figure 16. Typical microscopic morphology of oblique fracture fragments. (**a**) Step wiping and flower wiping; (**b**) Step wiping and flower wiping; (**c**) Parallel stripe pattern; (**d**) Transgranular pull flowers.

4.2. Failure Mechanism Analysis

The analysis of the SEM results shows that the flake spalling fragments and vertical fracture surface are mainly caused by the tensile failure mechanism and there are shear failure characteristics in some parts. The micromorphology of the fracture is mainly transgranular and intergranular drawing and step patterns. The fracture is clean and has less powder and the micromorphology of the inclined fracture surface is due to the shear failure mechanism. The broken mineral particles and powders on the fracture surface can be seen everywhere. Combined with the deformation, failure, and strength characteristics of rock samples under different confining pressures, the following was seen:

(1) The triaxial compression test was carried out under the condition of low confining pressure. The granite sample with the maximum free water absorption predominantly experienced brittle failure. The microcracks extended from both opposite ends towards the middle where they finally connected. At this point, the rock sample instantly lost its bearing capacity, collapsed loudly, and produces mostly vertical fracture surfaces and flake spalling fragments. Combining this information with the SEM data, the failure mechanism is found to be comprehensive tensile and shear failure, with predominantly tensile failure.

(2) Triaxial compression tests were performed under medium and high confining pressures. The granite sample with the maximum free water absorption experienced mainly plastic failure. After failure, it mainly produced an inclined fracture surface and sometimes a conjugate shear surface. The integrity of the sample after failure was good. Combined with the SEM results, the failure mechanism was shown to be tensile and shear comprehensive failure, with mainly shear failure and some localized tensile failure.

5. Conclusions

The mechanical properties of granite with maximum free water absorption under different confining pressures were studied through triaxial compression tests. The failure mechanism of granite was analyzed through the macro failure characteristics and micromorphology of the granite. The main conclusions are as follows:

(1) The maximum free water absorption of this type of granite is between 0.180 and 0.204%. The free water absorption of granite changes greatly within the first 42 h, increasing from 0% to approximately 0.150%. From 306 h to 546 h, the free water absorption of the rock sample is negligible. Therefore, the water absorption test was stopped after 546 h. The P-wave velocity was between 3300 and 4900 m/s and the variation law of the P-wave velocity was basically consistent with that of water absorption. According to the water immersion test and wave velocity measurement results of the rock samples, the samples reached maximum free water absorption after 546 h.

(2) The differential stress-axial strain curve can be divided into the initial compaction stage, the elastic compaction stage, the plastic deformation stage before the peak, and the residual stage after the peak. With the increase in confining pressure, the initial compaction stage becomes increasingly smaller. That is, the specimen becomes increasingly dense under the action of confining pressure and with an increase in confining pressure, the plastic deformation stage before the peak becomes longer, indicating that the plasticity of the sample is obvious with the increase in confining pressure and the peak strength and peak displacement also increase with the increase in confining pressure. The elastic modulus increases significantly at the beginning and then increases slowly. The increase in confining pressure increases the strength of the rock mass.

(3) When the confining pressure is in the range of 0–20 MPa, the peak axial stress of the granite with the maximum free water absorption rate is between 146.0 and 307.6 MPa and the elastic modulus is between 31.36 and 44.18 GPa. It increased linearly with confining pressure. Using the Mohr–Coulomb strength criterion, the c value of the rock was calculated to be 26.84 MPa and the φ value was 51°. From the Hoek–Brown strength criterion, the strength parameter s representing the granite rock mass is 1, m is 21.42, and α is 0.499.

(4) Through research on the failure characteristics and fracture surface morphology of granite triaxial compression under different confining pressures, it was found that under low confining pressure conditions, the vertical fracture surface is the main one, and the inclination angle of the fracture surface gradually decreases with the increase in the confining pressure. Under medium and high confining pressures, the inclined fracture surface was dominant.

(5) The microscopic morphology of the flake-like exfoliated fragments and the fracture surface showed that they were mainly tensile fractures with partial shear failures, while the inclined fracture surfaces were mainly shear failures with partial tensile failures. Under the condition of low confining pressure, the main failure mechanism is tensile failure. The inclined fracture surface is mostly generated under medium and high confining pressures, where the main failure mechanism is shear failure.

Author Contributions: Conceptualization and methodology, Y.C. (Yangbing Cao); validation, formal analysis, investigation, Y.Z., Y.C. (Yangtao Chen) and Z.L.; Data curation, Z.H.; writing—original draft preparation, Y.Z. and Y.C. (Yangtao Chen); writing—review and editing, Y.Z., Z.L. and Y.C. (Yangbing Cao); visualization, Y.Z. and Y.C. (Yangtao Chen); supervision and project administration, Y.C. (Yangbing Cao); funding acquisition, Y.C. (Yangbing Cao). All authors have read and agreed to the published version of the manuscript.

Funding: This research was funded by the Natural Science Foundation of Fujian Province of China (Grant No. 2019J05036), and by the Opening Fund of Key Laboratory of Geohazard Prevention of Hilly Mountains, Ministry of Natural Resources (Fujian Key Laboratory of Geohazard Prevention) (Grant No. FJKLGH2022K002).

Institutional Review Board Statement: Not applicable.

Informed Consent Statement: Not applicable.

Data Availability Statement: The data used to support the findings of this study are available from the corresponding author upon request.

Conflicts of Interest: The authors declare no conflict of interest.

References

1. Yang, P.Y.; Wu, X.; Chen, J. Elastic and plastic-flow damage constitutive model of rock based on conventional triaxial compression test. *Int. J. Heat Technol.* **2018**, *36*, 927–935. [CrossRef]
2. Xie, S.J.; Lin, H.; Chen, Y.F.; Wang, Y.X. A new nonlinear empirical strength criterion for rocks under conventional triaxial compression. *J. Cent. South Univ.* **2021**, *28*, 1448–1458. [CrossRef]

3. Zhou, H.; Meng, F.Z.; Liu, H.T.; Zhang, C.Q.; Lu, J.J.; Xu, R.C. Experimental study on characteristics and mechanism of brittle failure of granite. *Chin. J. Rock Mech. Eng.* **2014**, *33*, 1822–1827.
4. Lajtai, E.Z. Microscopic fracture processes in a granite. *Rock Mech. Rock Eng.* **1998**, *31*, 237–250. [CrossRef]
5. Chen, G.; Wang, J.; Li, J.; Li, T.; Zhang, H. Influence of temperature on crack initiation and propagation in granite. *Int. J. Geomech.* **2018**, *18*, 04018094. [CrossRef]
6. Zhu, Z.Q.; Sheng, Q.; Leng, X.L.; Zhu, F.G. Experimental study of dynamic mechanical property of Dagangshan granite. *Chin. J. Rock Mech. Eng.* **2010**, *29*, 3469–3474.
7. Du, S.J.; Liu, H.; Zhi, H.T.; Chen, H.H. Testing study on mechanical properties of post-high-temperature granite. *Chin. J. Rock Mech. Eng.* **2004**, *23*, 2359–2364.
8. Du, S.J.; Ma, M.; Chen, H.H.; Qiu, Y.Q. Testing study on longitudinal wave characteristics of granite after high temperature. *Chin. J. Rock Mech. Eng.* **2003**, *22*, 1803–1806.
9. Du, S.J.; Zhi, H.T. Experimental research on the mechanical properties of granite rock and concrete after high-temperature. *Chin. J. Geotech. Eng.* **2004**, *26*, 482–485.
10. Yao, W.; Cai, Y.Y.; Yu, J.; Zhou, J.F.; Liu, S.Y.; Tu, B.X. Experimental and numerical study on mechanical and cracking behaviors of flawed granite under triaxial compression. *Measurement* **2019**, *145*, 573–582. [CrossRef]
11. Yang, S.Q.; Huang, Y.H. An experimental study on deformation and failure mechanical behavior of granite containing a single fissure under different confining pressures. *Environ. Earth Sci.* **2017**, *76*, 364. [CrossRef]
12. Huang, Y.H.; Yang, S.Q. Mechanical and cracking behavior of granite containing two coplanar flaws under conventional triaxial compression. *Int. J. Damage Mech.* **2019**, *28*, 590–610. [CrossRef]
13. Zhao, X.G.; Ma, L.K.; Su, R.; Wang, J. Fracture evolution and strength characteristics of Beishan deep granite under compression conditions. *Chin. J. Rock Mech. Eng.* **2014**, *33*, 3665–3675.
14. Sun, X.; Li, E.B.; Duan, J.L.; Pu, S.K.; Tan, Y.H.; Han, Y.; Zhao, Y.Q. Study on acoustic emission characteristics and damage evolution law of Beishan granite under triaxial compression. *Chin. J. Rock Mech. Eng.* **2018**, *37*, 4234–4244.
15. Li, P.F.; Zhao, X.G.; Guo, Z.; Ma, L.K.; Chen, L.; Wang, J. Variation of strength parameters of Beishan granite under triaxial compression. *Chin. J. Rock Mech. Eng.* **2017**, *36*, 1599–1610.
16. Wang, C.L.; Du, G.Y.; Li, E.B.; Sun, X.; Pan, Y. Evolution of strength parameters and energy dissipation of Beishan deep granite under conventional triaxial compression. *Chin. J. Rock Mech. Eng.* **2021**, *40*, 2238–2248.
17. Dai, B.; Zhao, G.Y.; Konietzky, H.; Wasantha, P.L.P. Experimental investigation on damage evolution behaviour of a granitic rock under loading and unloading. *J. Cent. South Univ.* **2018**, *25*, 1213–1225. [CrossRef]
18. Ji, H.G.; Lu, X. Characteristics of acoustic emission and rock fracture precursors of granite under conventional triaxial compression. *Chin. J. Rock Mech. Eng.* **2015**, *34*, 694–702.
19. Chen, J.T. Experimental study on triaxial compression deformation and acoustic emission property of rock. *J. Wuhan Univ. Technol.* **2008**, *30*, 102–104.
20. Lee, B.; Rathnaweera, T.D. Stress threshold identification of progressive fracturing in Bukit Timah granite under uniaxial and triaxial stress conditions. *Geomech. Geophys. Geo-Energy Geo-Resour.* **2016**, *2*, 301–330. [CrossRef]
21. Wang, T.Z.; Wang, L.X.; Xue, F.; Xue, M.Y. Identification of crack development in granite under triaxial compression based on the acoustic emission signal. *Int. J. Distrib. Sens. Netw.* **2021**, *17*, 1550147720986116. [CrossRef]
22. Wang, W.; Liu, T.G.; Li, X.H.; Wang, P.B.; Xu, W.Y. Mechanical behaviour of granite in triaxial compression under chemical corrosion. *J. Cent. South Univ. (Sci. Technol.)* **2015**, *46*, 3801–3807.
23. Sun, C.; Zhang, S.G.; Jia, B.X.; Wu, Z.Q. Physical and numerical model tests on post-peak mechanical properties of granite. *Chin. J. Geotech. Eng.* **2015**, *37*, 847–852.
24. Li, L.; Tsui, Y.; Lee, P.K.K.; Tham, L.G.; Li, T.J.; Ge, X.R. Progressive cracking of granite plate under uniaxial compression. *Chin. J. Rock Mech. Eng.* **2002**, *21*, 940–947.
25. Zhang, H.J.; Li, C.C. Effects of confining stress on the post-peak behaviour and fracture angle of Fauske marble and Iddefjord granite. *Rock Mech. Rock Eng.* **2019**, *52*, 1377–1385. [CrossRef]
26. Cheng, H.; Zhou, X.P.; Zhu, J.; Qian, Q.H. The effects of crack openings on crack initiation, propagation and coalescence behavior in rock-like materials under uniaxial compression. *Rock Mech. Rock Eng.* **2016**, *49*, 3481–3494. [CrossRef]
27. Cheng, H.; Zhou, X.P. New Technique for frictional contact on crack slip in the extended finite-element method framework. *J. Eng. Mech.* **2018**, *144*, 04018059. [CrossRef]
28. Cheng, H.; Zhou, X.P.; Pan, X.K.; Berto, F. Damage analysis of sandstone during the creep stage under the different levels of uniaxial stress using NMR measurements. *Fatigue Fract. Eng. Mater. Struct.* **2020**, *44*, 719–732. [CrossRef]
29. Masuda, K. Effects of water on rock strength in a brittle regime. *J. Struct. Geol.* **2001**, *23*, 1653–1657. [CrossRef]
30. Li, U.; Zhu, W.S.; Bai, S.W.; Yang, C.H. Uniaxial experimental study on rheological properties of granite in air-dried and saturated states. *Chin. J. Rock Mech. Eng.* **2003**, *22*, 1673–1677.
31. Deng, C.F.; Liu, J.F.; Chen, L.; Li, Y.; Xiang, G. Mechanical behaviors and acoustic emission characteristics of fracture of granite under different moisture conditions. *Chin. J. Geotech. Eng.* **2017**, *39*, 1538–1544.
32. Cao, Y.B.; Chen, Y.H.; Huang, Z.P.; Liu, C.Y.; Qiu, D.D. Study on evaluation index of brittleness characteristics of granite under different water content conditions. *J. Eng. Geol.* **2020**, *28*, 29–38.

33. Cao, Y.B.; Chen, Y.H.; Zhang, P.; Huang, Z.P.; Zhang, X.X.; Chen, Y.T. Failure characteristics and mechanism of biotite monzogranite with different water content under uniaxial compression. *Bull. Geol. Sci. Technol.* **2021**, *40*, 163–172.
34. *GB/T 50266-2013*; Standard for Test Methods of Engineering Rock Mass. Ministry of Construction P.R.CHINA and China State Bureau of Quality and Technical Supervision (CSBTS): Beijing, China, 2013.
35. Li, X.W.; Lan, Y.R.; Zou, J.X. A study of rock fractures. *J. China Inst. Min. Technol.* **1983**, *1*, 18–24.
36. Liu, X.M.; Lee, C.F. Microfailure mechanism analysis and test study for rock failure surface. *Chin. J. Rock Mech. Eng.* **1997**, *16*, 509–513.
37. Feng, T.; Xie, X.B.; Pan, C.L.; Guo, R. Fracture mechanism analysis for burst rock with electron scanning microscope. *J. Cent. South Univ.* **1999**, *30*, 14–17.
38. Zhao, K.; Zhao, H.Y.; Jia, Q.Y. An analysis of rockburst fracture micromorphology and study of its mechanism. *Explos. Shock. Waves* **2015**, *35*, 913–918.
39. Zheng, D.; Ju, N.P. Scanning electronic microscope tests for rock micro-rupture mechanism and fracture characteristic of phyllite. *J. Eng. Geol.* **2011**, *19*, 317–322.
40. Cui, Z.D.; Han, W.G. In situ scanning electron microscope (SEM) observations of damage and crack growth of shale. *Microsc. Microanal.* **2018**, *24*, 107–115. [CrossRef]